Electrically-pumped, broad-area, single-mode photonic crystal lasers

Lin Zhu, Philip Chak, Joyce K.S. Poon, Guy A. DeRose, Amnon Yariv and Axel Scherer

Department of Electrical Engineering and Department of Applied Physics, California Institute of Technology, Pasadena, CA 91125

linz@caltech.edu

http://www.its.caltech.edu/ linz

Abstract: Planar broad-area single-mode lasers, with modal widths of the order of tens of microns, are technologically important for high-power applications and improved coupling efficiency into optical fibers. They may also find new areas of applications in on-chip integration with devices that are of similar size scales, such as for spectroscopy in microfluidic chambers or optical signal processing with micro-electromechanical systems. An outstanding challenge is that broad-area lasers often require external means of control, such as injection-locking or a frequency/spatial filter to obtain single-mode operation. In this paper, we propose and demonstrate effective index-guided, large-area, edge-emitting photonic crystal lasers driven by pulsed electrical current injection at the optical telecommunication wavelength of 1550nm. By suitable design of the photonic crystal lattice, our lasers operate in a single mode with a $1/e^2$ modal width of 25μm and a length of 600μm .

OCIS codes: (140.5960) Semiconductor lasers; (350.2770) Gratings; (130.2790) Guided waves.

References and links

1. A. Yariv, and P. Yeh, *Optical Waves in Crystals: Propagation and Control of Laser Radiation.* (Wiley, New York, 1984)
2. S. John,"Strong localization of photons in certain disordered dielectric superlattices," Phys. Rev. Lett., **58**, pp. 2486–2489 (1987)
3. E. Yablonovitch, "Inhibited spontaneous emission in solid-state physics and electronics," Phys. Rev. Lett., **58**, pp. 2059–2062 (1987)
4. O. Painter, R. K. Lee, A. Scherer, A. Yariv, J. D. O'Brien, P. D. Dapkus, and I. Kim, "Two-Dimensional Photonic Band-Gap Defect Mode Laser," Science, **284**, pp. 1819–1821 (1999)
5. S. Noda, M, Yokoyama, M. Imada, A. Chutinan, and M. Mochizuki, "Polarization mode control of two-dimensional photonic crystal laser by unit cell structure design," Science, **293**, pp. 1123–1125 (2001)
6. R.Colombelli, K. Srinivasan, M. Troccoli, O. Painter, C. F. Gmachl, D. M. Tennant, A. M. Sergent, D. L. Sivco, A. Y. Cho, and F. Capasso, "Quantum cascade surface-emitting photonic crystal laser," Science, **302**, pp. 1374–1377 (2003)
7. H. G. Park, S. H. Kim, S. H. Kwon, Y. G. Ju, J. K. Yang, J. H. Baek, S. B. Kim, and Y. H. Lee, "Electrically driven single-cell photonic crystal laser," Science, **305**, pp. 1444–1447 (2004)
8. L. Zhu, J. M. Choi, G. A. DeRose, A. Yariv, and A. Scherer, "Electrically pumped two-dimensional Bragg grating lasers," Opt. Lett., **31**, pp. 1863–1865 (2006)
9. J. C. Knight, and P. ST. J. Russell, "New ways to guide light," Science, **296**, pp. 276–277 (2002)
10. T. A. Birks, J. C. Knight, and P. ST. J. Russell, "Endlessly single-mode photonic crystal fiber," Opt. Lett., **22**, pp. 961–963 (1997)

#80730 - $15.00 USD Received 7 Mar 2007; revised 20 Apr 2007; accepted 28 Apr 2007; published 1 May 2007

11. E. Schwoob, H. Benisty, C. Weisbuch, C. Cuisin, E. Derouin, O. Drisse, G. H. Duan, L. Legouezigou, O. Legouezigou, and F. Pommereau, "Enhanced gain measurement at mode singularities in InP-based photonic crystal waveguides," Opt. Express, **8**, pp. 1569–1574 (2004)
12. T. D. Happ, M. Kamp, A. Forchel, J .L. Gentner, and L. Goldstein, "Two-dimensional photonic crystal coupled-defect laser diode," Appl. Phys. Lett., **82**, pp. 4–6 (2003)
13. S. G. Johnson, and J. D. Joannopoulos, "Block-iterative frequency-domain methods for Maxwell's equations in a planewave basis," Opt. Express, **8**, pp. 173–190 (2004)
14. R. F. Kazarinov, and C. H. Henry, "Second-order distributed feedback lasers with mode selection provided by first-order radiation losses," IEEE J. Quantum Electron., **QE21**, pp. 144–150 (1985)
15. H. Wenzel, R. Guther, A. M. Shams-Zadeh-Amis, and P. Biensturan, "A comparative study of higher order Bragg gratings : couple-mode theory versus mode expansion modelling," IEEE J. Quantum Electron., **QE46**, pp. 64–70 (2006)
16. G. A. DeRose, L. Zhu, J. M. Choi, J. K. S. Poon, A. Yariv and A. Scherer, "Two-dimensional Bragg Grating Lasers Defined by Electron-Beam Lithography," J. Vac. Sci. Technol. B, **24**, pp. 2926–2930 (2006)
17. W. Green, J. Scheuer, G. A. DeRose, and A. Yariv, "Vertically emitting annular Bragg lasers using polymer epitaxial transfer," Appl.Phys. Lett., **85**, pp. 3669–3671 (2004)

1. Introduction

For more than three decades, structures with spatially periodic dielectric constants have played a crucial role in engineering the propagation and confinement of optical waves [1]. More recently, photonic crystals, which typically refer to structures with periodicities in two or more dimensions, have garnered significant interest [2]·[3]. Chip-scale photonic crystals are usually fabricated in high refractive index contrast material systems (e.g. semiconductor with air holes) for the tight confinement of the optical field beyond the limits of total internal reflection. In particular, photonic crystal defect cavity lasers have been demonstrated as highly compact, coherent sources of light [4]. However, to achieve the large index contrast required by these devices, suspended membranes are often required, making these lasers structurally less robust and rendering the problem of heat dissipation. In consequence, there have been relatively few reports of electrically driven photonic crystal lasers [5]·[6]·[7]·[8], which are essential for the optoelectronic integration of photonic crystal devices.

Most on-chip photonic crystal lasers to date use Bragg reflection to select the lasing mode and are vertically emitting. In general, photonic crystal structures can support two different kinds of modes: Bragg-guided and effective index-guided. For Bragg-guided modes, light is confined by Bragg reflection arising from a photonic bandgap in the transverse directions [9]. Electrically pumped semiconductor photonic crystal lasers with Bragg-guided modes have been demonstrated in surface emitting structures with both low index contrast [5] and high index contrast [7]. In our previous work [8], we have shown some preliminary results of electrically pumped, edge-emitting semiconductor lasers with cross defects based on Bragg-guided modes. For effective index-guided modes, confinement in the transverse direction is due to the index difference between the core and the effective medium formed by the periodic structure in the cladding. In photonic crystal fibers, the effective index guiding mechanism can be used to design single-mode fibers with large modal areas over a wide range of wavelengths [10].

In this work, we describe photonic crystal lasers with low index contrast that operate under a pulsed electrical current injection. These are edge-emitting devices and are well-suited for planar integration. We show that it is possible to find a regime where effective index guiding and Bragg reflection couple strongly resulting in a hybrid mode with a large volume and reduced group velocity and thus an enhanced gain. In contrast to conventional distributed feedback (DFB) lasers, the lasing mode frequency is away from the Brillouin zone edge of the photonic crystal [11]·[12].

#80730 - $15.00 USD Received 7 Mar 2007; revised 20 Apr 2007; accepted 28 Apr 2007; published 1 May 2007

2. Results

2.1. Laser design and fabrication

Figure 1 shows a schematic of our two dimensional photonic crystal laser. The surface structure consists of a rectangular lattice array of polymer-filled holes with a waveguide core on the wafer surface. The active multiple-quantum-well layers are underneath the photonic crystal layer. The photonic crystal lattice consists of about $\sim 10^6$ nanoscale holes each with a radius of 100nm. Light is confined in the vertical direction by total internal reflection. The size of the electrical contact is $600\mu\text{m} \times 160\mu\text{m}$ (length $\times$ width). The refractive index contrast between the etched hole and unetched region is on the order of 10^{-2}, which is about two orders of magnitude smaller than conventional photonic crystals but also two orders of magnitude larger than a single-mode step-index waveguide of comparable dimensions.

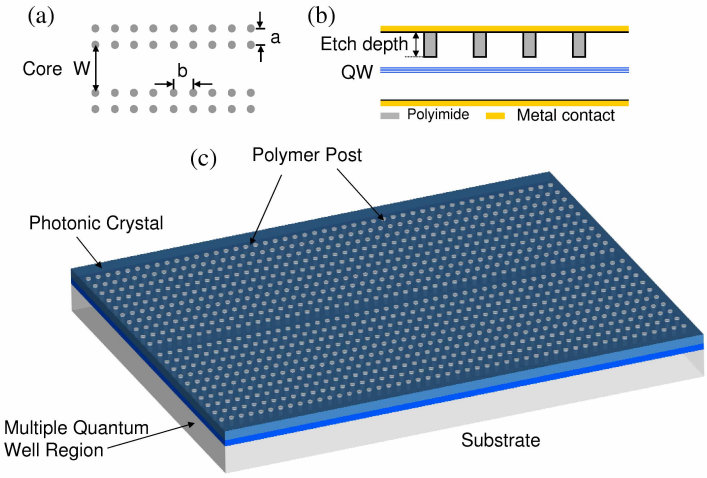

Fig. 1. **Schematic of a fabricated photonic crystal laser with a waveguide core.** (a) a is the transverse lattice constant, b is the longitudinal lattice constant, and W is the core width. (b) The cross section structure. (c) Planar geometry of the photonic crystal lasers, with gain provided by the multiple quantum well layers.

The fabrication procedure consists of a series of lithography, etching, planarization, and metallization steps (see also the Appendix). First, the photonic crystal lattice is defined using electron-beam lithography and etched into the surface of the wafer. The etch depth of 410nm is chosen to obtain the desired refractive index contrast and avoid etching through the quantum-wells. Next, we planarize the structure by depositing a layer of polyimide and etching it back until the device surface is exposed. The planarization is necessary to reduce the optical losses from the metallic contacts and to obtain good contact quality. The top (p-side) contact is then deposited onto the lasers by metal evaporation and lift-off. The devices are then mechanically thinned, and the n-side contact is deposited. Finally the laser bars are separated from the wafer by cleaving. Figure 2 shows scanning electron microscope (SEM) images of a photonic crystal laser after the polyimide planarization.

We fabricate lasers with various lattice constants and core widths and test them at room temperature in pulsed operation without active cooling. Current pulses with a duration of 100ns and a period of 10μs are injected to drive the lasers (see also the Appendix). Single-mode lasing, with a single peak in the spectrum, a single lobe in the near-field profile, and a diffraction-

#80730 - $15.00 USD Received 7 Mar 2007; revised 20 Apr 2007; accepted 28 Apr 2007; published 1 May 2007

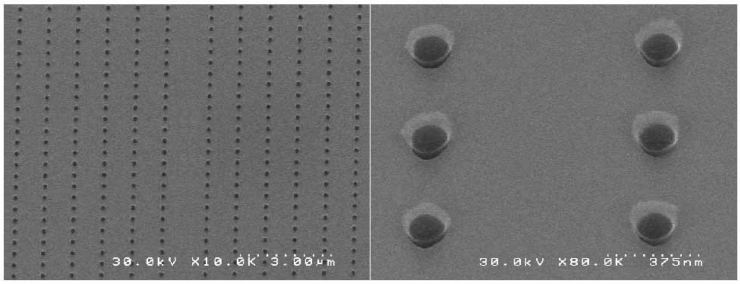

Fig. 2. **Scanning electron-microscope images of a polymer-planarized two-dimensional photonic crystal laser.** (a) Rectangular array of etched holes with a waveguide core. (b) Polyimide-filled holes each with a radius of 100nm. The images are taken before the deposition of electrical contacts.

limited far-field pattern, is achieved. First, we test a set of lasers with a transverse lattice constant, a, of 1μm, core width of 1.5μm, and longitudinal lattice constant, b, ranging from 400nm to 500nm in 20nm steps. Single-mode lasing is observed for $b = 400$nm. To explore this effect in greater detail, we next test two sets of lasers with $a = 1\mu$m and $a = 0.8\mu$m, with waveguide core widths of 1.5μm and 1.2μm, respectively. For each set of lasers, b is varied from 390nm to 410nm in 10nm steps.

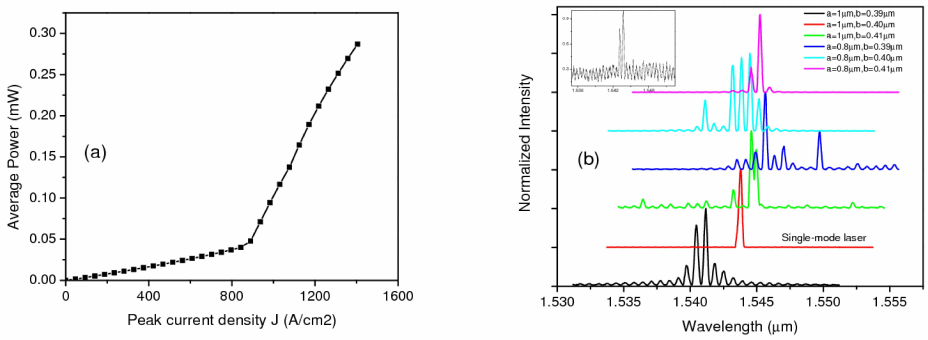

Fig. 3. **(a)The L-I curve of the structure with $a = 1.0\mu$m and $b = 400nm$. (b)Lasing spectra above the threshold (with $J = 1.1J_{th}$) for structures with different lattice constants.** Single-mode operation is observed for the structure with $a = 400nm$ and $b = 1.0\mu$m. The inset shows the spectrum for the single mode laser near threshold.

2.2. Measurements of the L-I curve and lasing spectra

Figure 3 (a) shows the light-current density curve (average power verse peak current density) for the PC laser with $a = 1.0\mu$m and $b = 400nm$. It has a clear threshold around $890\text{A}/\text{cm}^2$. Using the fact that light is only collected from one facet and the duty cycle of the current pulse is 0.01, we calculate a slope efficiency of $0.1W/A$ (average power verse average current). Other lasers with different lattice constants have similar L-I curves with clear thresholds. Figure 3

#80730 - $15.00 USD Received 7 Mar 2007; revised 20 Apr 2007; accepted 28 Apr 2007; published 1 May 2007

(b) shows the measured optical spectra for different photonic crystal lattices. These spectra are obtained for devices on the same cleaved bar under the identical pump current density level $J = 1.1J_{th}$. The laser with $a = 1\mu$m and $b = 400nm$ shows a single peak in the lasing spectrum, while the other lasers exhibit multiple peaks. The side mode suppression ratio for the single-mode laser is about 30dB. We also have measured the single-mode lasing spectrum at different positions along the emitting facets and obtained the same results. For the multi-mode lasers, the free spectral range (FSR) is about 0.6nm, in agreement with a laser length of $600\mu m$. The FSR suggests that these emission peaks arise from the longitudinal modes of the laser defined by end facets. The lasing wavelength for the single-mode laser is near 1543.8nm, while the highest lasing peaks for other two lasers with the same transverse periodicity but a different longitudinal period are around 1541.2nm and 1544.8nm respectively. This indicates the lasing wavelength is determined by the lattice geometry of the photonic crystal rather than the material gain spectrum. The spectrum of the single-mode laser has two very closly spaced peaks near threshold, similar to a DFB laser. As the pump current increases, the mode at the longer wavelength (1543.8nm) dominates. The single-mode behavior is maintained until $J = 1.5J_{th}$.

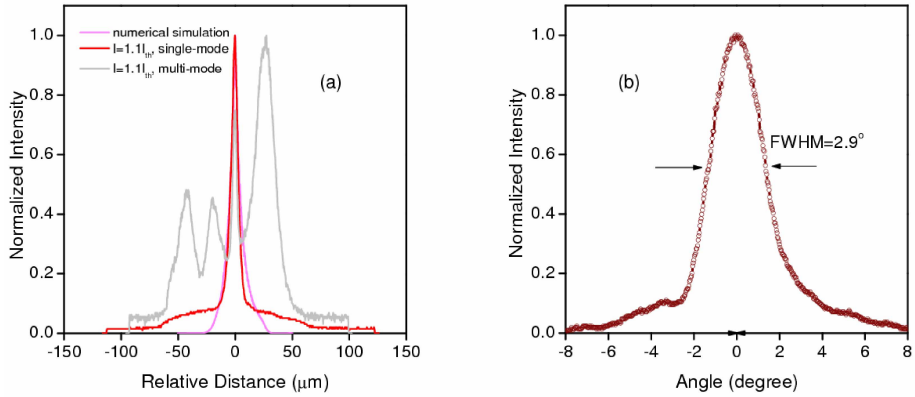

Fig. 4. **Near- and far- field profiles for the measured photonic crystal lasers.** (a) Experimentally observed near-field profiles for the single-mode (red line) and a multi-mode structure (gray line) above threshold. For comparison, a numerically calculated near-field profile is also shown (purple line). For this simulated mode, the $1/e^2$ modal width is approximately 26μm , which matches closely with the experimentally observed value of 25μm (b) Experimentally observed far-field pattern. The far-field single lobe has a FWHM of 2.9^o.

2.3. Measurements of the lasing near- and far- fields

Figure 4 (a) shows near-field profiles for some tested devices above the threshold. As shown in Fig. 4 (a), the near-field of the single-mode laser has a clear single lobe centered at the core in the middle of the metal contact, which suggests that only one transverse mode exists. The $1/e^2$ modal width from the near-field profile is $\sim 25\mu$m. In contrast, the multi-mode lasers have multiple lobes along the cleaved facet including the lobe at the core. Multi-lobed near-field profiles are always accompanied by a multi-peaked laser spectra, which indicates that more than one transverse mode can oscillate in the multi-mode lasers.

In addition to the single lasing peak and the single-lobed near-field, the single-mode laser

#80730 - $15.00 USD Received 7 Mar 2007; revised 20 Apr 2007; accepted 28 Apr 2007; published 1 May 2007

also possesses a diffraction-limited single-lobed far-field pattern with a divergence angle of 2.9^o. The measured far-field profile for this laser is shown in Fig. 4 (b) and it is similar to that of a large-area index-guided ridge waveguide mode. This implies effective index, rather than Bragg reflection is the main waveguiding mechanism for the lasing mode.

Since the contact width is bigger than the lasing modal width, there are some tails in both the near-field and far-field profiles. We also expect more robust and efficient single-mode output if we match the contact with the lasing modal width.

2.4. Numerical simulations of the single-mode photonic crystal laser

In general, the effective index guiding mechanism alone does not guarantee single-mode operation since all of the tested laser geometries support effective index-guided modes. To explain quantitatively the single-mode lasing spectrum in Fig. 3, we employ a two dimensional frequency-domain supercell method [13] and numerically solve for modes that are localized in the core. Our supercell consists of 50 photonic crystal unit cells on each side of the core, with the same geometry as the single-mode laser. Since the multi-layer quantum well structures give preferential gain to TE modes of our system, we restrict ourselves to TE modes (H-field out-of-plane) in the simulation.

The results from the simulation are summarized in Fig. 5. The dispersion curve of index-guided modes is shown in Fig. 5 (a) (red circle). It has a mini-bandgap, with details shown in the inset, in close vicinity of $b/\lambda \simeq 0.2535$, which is approximately corresponding to the lasing wavelength of the single-mode laser. The black dotted lines in Fig. 5 (a) represent the band structure of the photonic crystal cladding (the photonic crystal structure without the defect core). Fig. 5 (b) and (c) show the associated H-fields at various points of the dispersion curve. Around the mini-gap the field is delocalized (Fig. 5 (c)) and the group velocity is reduced (Fig. 5 (d)). It is the reduction of group velocity around the mini-bandgap that contributes to the single-mode lasing observed in Fig. 3.

The origin of the mini-bandgap of the dispersion curve of index-guided modes is the coupling between effective index-guided modes and a particular order of Bragg reflection from the cladding photonic crystal. For modes away from the mini-bandgap in Fig. 5 (a), such as at points (1) and (3), the field profiles have a main lobe slowly varying on the scale of the unit cell and thus resemble fundamental ridge waveguide modes. Within the simplest approximation, these modes can be described as plane waves with no transverse components. In the vicinity of the mini-bandgap, this plane wave is scattered by the photonic crystal cladding. The scattering process is best illustrated using the band structure of the cladding photonic crystal. At the Bloch wavenumber $K_x = 0$, the dispersion relation of the photonic crystal cladding (dotted lines in Fig. 5 (a)) shows that near the frequency of the mini-bandgap of the photonic crystal waveguide dispersion relation, there is an anti-crossing between the photonic crystal bands.

Physically, this anti-crossing corresponds to the situation where the forward/backward propagating plane wave is scattered sideways. In the limit of weak coupling, the cladding dispersion curve in Fig. 5 (a) consists of lines with $b/\lambda = (b/2\pi)\left|(2\pi p/a)\hat{x} + (2\pi q/b + K_y)\hat{y}\right|$ (where K_y is the Block wavenumber in the y direction and p,q are integers) and small anti-crossings between them. Around the mini-bandgap, the phase-matching condition is satisfied as plane waves with wavevector $\vec{k} = (-2\pi/b + K_y)\hat{y}$ and $\vec{k} = (\pm 4\pi/a)\hat{x} + (K_y)\hat{y}$ are coupled by the reciprocal lattice vectors $\vec{G} = \pm(4\pi/a)\hat{x} \pm (2\pi/b)\hat{y}$). Detailed discussions are included in the Appendix.

3. Discussion

For the structures with different geometries in Fig. 3, the location of the mini-gap will be at a different frequency. As a result, the reduction in group velocity will be at a frequency that is

#80730 - $15.00 USD Received 7 Mar 2007; revised 20 Apr 2007; accepted 28 Apr 2007; published 1 May 2007

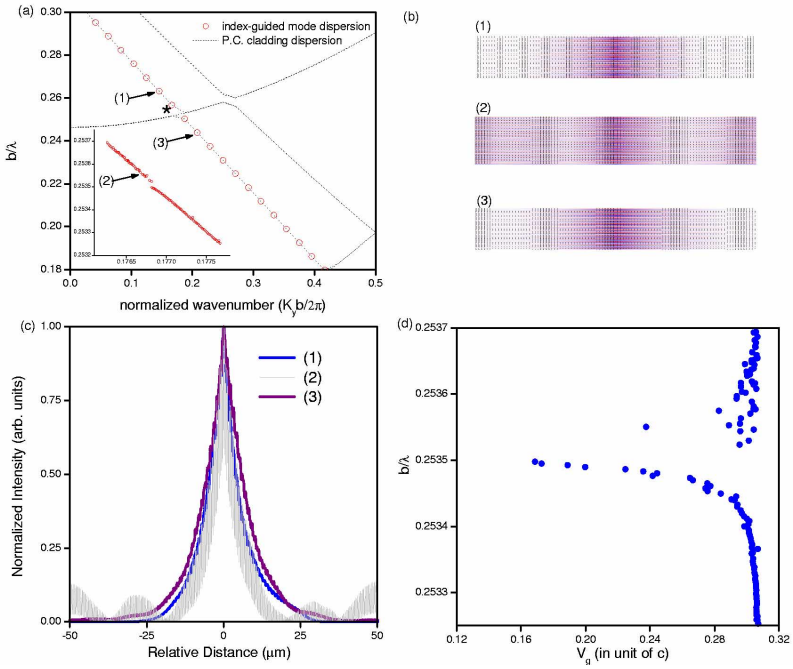

Fig. 5. **Simulation results for the single-mode photonic crystal laser structure.** (a) Dispersion relation of effective-index guided modes (circles) superimposed on dispersion relation of the cladding photonic crystal (dotted lines). The inset shows the detail around the bandgap of the dispersion of index guided modes (b),(c)The out of plane component of the magnetic field profiles at various points of the dispersion curve (d) Group velocity of the effective index-guided modes in the vicinity of the mini-bandgap.

far away from the peak of the gain spectrum of the laser material. Thus, a single mode is not necessarily preferred for laser oscillation.

The feedback effect we have described differs from a conventional DFB laser. In a DFB, a grating couples a forward propagating index-guided mode couples to its backward propagating counterpart without adding any transverse component and the laser oscillates at the Brillouin zone edge ($K_y = \pi/b$). Operation at $\lambda_0 = 1.54\mu$m corresponds to a photonic crystal lattice with $b = 480$nm and $a = 1.0\mu$m when the second order Bragg reflection condition in the longitudinal direction is satisfied. However, single-mode lasing is not observed in that case, which may be attributed to multiple modes with similar gain at that Brillouin zone edge and the increased vertical out-of-plane loss accompanying the second order Bragg reflection [14],[15]. To achieve single-mode operation using conventional DFB feedback, first order Bragg gratings, which possess a shorter period and are thus more difficult to define lithographically, are necessary.

In summary, we have demonstrated a new type of electrically-pumped, edge-emitting, large-area photonic crystal lasers. Single-mode operation was achieved by combining the transverse confinement provided by an effective index-guiding mechanism with the longitudinal mode selection provided by the Bragg reflection from the photonic crystal cladding. Our devices represent important first step toward using photonic crystals in a different way for modal control in planar optical circuits.

#80730 - $15.00 USD Received 7 Mar 2007; revised 20 Apr 2007; accepted 28 Apr 2007; published 1 May 2007

Acknowledgment

L. Zhu thanks Oskar Painter and Raviv Perahia for providing access to their PECVD facility. The work was supported by the Defense Advanced Research Projects Agency (M. Stickley). P. Chak and J. Poon are grateful for the financial support from the Natural Sciences and Engineering Research Council of Canada.

#80730 - $15.00 USD Received 7 Mar 2007; revised 20 Apr 2007; accepted 28 Apr 2007; published 1 May 2007

Appendix

Fabrication

We fabricate our lasers in commercially grown active semiconductor materials. The semiconductor material has InGaAsP layers totaling a thickness of 725nm on top of an InP substrate. Optical gain is provided by four 8.5nm thick unstrained InGaAsP quantum wells which are separated by 10nm InGaAsP barriers. The quantum wells are located 625nm from the top of the wafer surface. The active quaternary material is designed to emit light at around 1548nm.

The epitaxially grown material is first coated with a 120nm plasma-enhanced chemical vapor deposition (PECVD) silica (SiO_2) hard mask layer and a 250nm polymethylmethacrylate (PMMA) resist layer. We expose PMMA in a Leica Microsystems EBPG 5000+ electron beam-writer at 100 kV. Proximity effect correction is used for the electron beam lithography to obtain a uniform pattern distribution over large areas [16]. After resist development, the PMMA patterns are transferred into the SiO_2 layer by reactive ion etching (RIE) using a CHF_3 plasma. The SiO_2 layer then serves as a hard mask to etch the semiconductor using an inductively coupled plasma RIE (ICP-RIE) with HI/Ar chemistry [17].

We then coat the devices with a 2μm thick polyimide (PI-2562, HD Microsystems) planarization layer. The polyimide is subsequently etched back to the SiO_2 layer by an ICP-RIE using oxygen (O_2). During this process, the SiO_2 layer provides additional 80 nm etch depth tolerance for the polyimide. After the polyimide etch, we strip off the remaining SiO_2 in buffered hydrofluoric acid solution creating a polyimide post inside each etched semiconductor hole. We can achieve a clean semiconductor surface without any polymer residue due to the SiO_2 isolation layer between the semiconductor and the polymer. P-type electrical contacts, Cr/AuZn/Au, are then thermally evaporated on the device. After mechanical thinning the substrate, n-type contacts, Cr/AuGe/Au, are evaporated on the backside. Finally, the laser bars are cleaved to lengths of about 600μm, and the facets are left uncoated.

Measurements

We test our lasers at room temperature in pulsed operation without active cooling. Current pulses from a HP 8114A pulse generator with a duration of 100ns and a period of 10μs are injected to drive the lasers. The output optical signal from the device is first collected by a $50\times$ microscope lens from the cleaved facet and is coupled into a multimode fiber. The optical spectrum is then measured by a HP 70951B optical spectrum analyzer with a maximum resolution of 0.08nm .

We take the near-field image of the test laser diode using the same $50\times$ microscope lens and an SUI SU640SDV infrared charge-coupled (CCD) camera. We use a micrometer stage to adjust the position of the lens between the laser and the camera. We directly measure the far-field pattern by putting the CCD camera in front of the laser without any imaging optics. The distance between the laser facet and the camera sensor plane is 8cm. The center of the acquired image represents the optical intensity at 0^o relative to the optical axis.

Wave coupling in the photonic crystal cladding

The mode coupling described in the article can be best illustrated using the band structure of a 2D photonic crystal with infinitesimally small index variation. The dispersion relation for an empty rectangular lattice (along the $\Gamma - M$ direction, $K_x = 0$) is shown in Fig. 6. The band structure consists of lines with

$$\omega(K_y) = \frac{c}{n_{avg}} \left| \left(\frac{2\pi p}{a} \right) \hat{x} + \left(\frac{2\pi q}{b} + K_y \right) \hat{y} \right|, \quad (1)$$

#80730 - $15.00 USD Received 7 Mar 2007; revised 20 Apr 2007; accepted 28 Apr 2007; published 1 May 2007

K_x and K_y are Bloch wavenumbers. In Eq. (1), c is the speed of light in vacuum, n_{avg} is the average refractive index for the photonic crystals, and a (b) is the transverse (longitudinal) lattice constant, and p,q are integers. Each line in Fig. 6 is associated with a particular pair of (p,q), and they represent planes waves with different wavevectors propagating inside the structure. For example, when $(p,q)=(0,0)$ we have $\omega=(c/n_{avg})|K_y|$, which represents plane waves propagating in the $\pm\hat{y}$ direction; when $(p,q)=(\pm1,0)$ we have $\omega=(c/n_{avg})\sqrt{(2\pi/a)^2+K_y^2}$, which represents planes waves with both forward ($\hat{y}$) and transverse ($\hat{x}$) components. At the crossing points of the dispersion relation, two (or more) modes with different wavevectors are coupled together, and phase matching conditions in space and time are satisfied simultaneously.

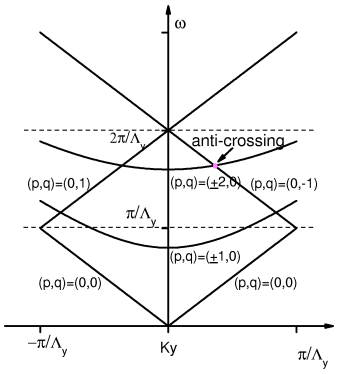

Fig. 6. Photonic crystal dispersion relation with the Bloch wavenumber $K_x=0$

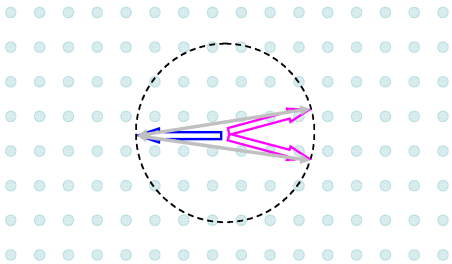

Fig. 7. Schematic of the coupling between different wavevectors. The backward propagating field (blue arrow) is coupled to the sideway propagating fields (purple arrows) by the reciprocal lattice vectors (gray arrows).

Of particular interest is the crossing denoted by the purple dot in Fig. 6, where plane waves with no transverse components (with $\omega=(c/n_{avg})(2\pi/b-K_y)$) are coupled to plane waves propagating sideways (with $\omega=(c/n_{avg})\sqrt{(4\pi/a)^2+K_y^2}$). This coupling is mediated by the lattice vectors $\vec{G}=(\pm4\pi/a)\hat{x}\pm(2\pi/b)\hat{y}$. We illustrate this coupling with the wavevector diagram shown in Fig. 7.

#80730 - $15.00 USD Received 7 Mar 2007; revised 20 Apr 2007; accepted 28 Apr 2007; published 1 May 2007